2013

Highly uniform TiO2/SnO2/carbon hybrid nanofibers with greatly enhanced lithium storage performance

Zunxian Yang
Fuzhou University

Qing Meng
University of Wollongong, qm982@uowmail.edu.au

Zaiping Guo
University of Wollongong, zguo@uow.edu.au

Xuebin Yu
Fudan University,University Of Wollongong, xyu@uow.edu.au

Tailiang Guo
Fuzhou University

See next page for additional authors

Publication Details

Yang, Z., Meng, Q., Guo, Z., Yu, X., Guo, T. and Zeng, R. (2013). Highly uniform TiO2/SnO2/carbon hybrid nanofibers with greatly enhanced lithium storage performance. Journal of Materials Chemistry A, 1 (35), 10395-10402.

Highly uniform TiO2/SnO2/carbon hybrid nanofibers with greatly enhanced lithium storage performance

Abstract
Highly uniform, relatively large area TiO2/SnO 2/carbon hybrid nanofibers were synthesized by a simple method based on thermal pyrolysis and oxidation of an as-spun titanium-tin/polyacrylonitrile nanoweb composite in an argon atmosphere. This novel composite features the uniform dispersion and encapsulation of highly uniform nanoscale TiO 2/SnO2 crystals in a porous carbon matrix. The high porosity of the nanofiber composite material, together with the conductive carbon matrix, enhanced the electrochemical performance of the TiO 2/SnO2/carbon nanofiber electrode. The TiO 2/SnO2/carbon nanofiber electrode displays a reversible capacity of 442.8 mA h g-1 for up to 100 cycles, and exhibits excellent rate capability. The results indicate that the composite could be a promising anode candidate for lithium ion batteries.

Keywords
hybrid, carbon, sno2, performance, highly, uniform, tio2, storage, lithium, enhanced, greatly, nanofibers

Disciplines
Engineering | Physical Sciences and Mathematics

Publication Details
Yang, Z., Meng, Q., Guo, Z., Yu, X., Guo, T. and Zeng, R. (2013). Highly uniform TiO2/SnO2/carbon hybrid nanofibers with greatly enhanced lithium storage performance. Journal of Materials Chemistry A, 1 (35), 10395-10402.

Authors
Zunxian Yang, Qing Meng, Zaiping Guo, Xuebin Yu, Tailiang Guo, and Rong Zeng

Journal of Materials Chemistry A

RSC Publishing

PAPER

View Article Online
View Journal | View Issue

Cite this: J. Mater. Chem. A, 2013, 1, 10395

Highly uniform TiO_2/SnO_2/carbon hybrid nanofibers with greatly enhanced lithium storage performance†

Zunxian Yang,*[a] Qing Meng,[b] Zaiping Guo,*[bc] Xuebin Yu,*[d] Tailiang Guo[a] and Rong Zeng[e]

Received 3rd May 2013
Accepted 24th June 2013

DOI: 10.1039/c3ta11751k

www.rsc.org/MaterialsA

Highly uniform, relatively large area TiO_2/SnO_2/carbon hybrid nanofibers were synthesized by a simple method based on thermal pyrolysis and oxidation of an as-spun titanium–tin/polyacrylonitrile nanoweb composite in an argon atmosphere. This novel composite features the uniform dispersion and encapsulation of highly uniform nanoscale TiO_2/SnO_2 crystals in a porous carbon matrix. The high porosity of the nanofiber composite material, together with the conductive carbon matrix, enhanced the electrochemical performance of the TiO_2/SnO_2/carbon nanofiber electrode. The TiO_2/SnO_2/carbon nanofiber electrode displays a reversible capacity of 442.8 mA h g^{-1} for up to 100 cycles, and exhibits excellent rate capability. The results indicate that the composite could be a promising anode candidate for lithium ion batteries.

1 Introduction

SnO_2, as one of the most important photoelectric functional materials, has drawn considerable attention due to its broad application in many fields, including gas sensors,[1] dye-sensitized solar cells,[2] catalysts,[3] field emission,[4] supercapacitors,[5] and especially, lithium ion batteries,[6–9] mainly due to its high gravimetric (780 mA h g^{-1}) and volumetric capacity.[10] Various tin oxide nanostructures, including nanospheres[11] and hollow microspheres,[7] as well as one-dimensional (1D) nanomaterials, such as nanofibers,[12–14] nanoribbons, nanowires[15,16] and nanorods,[17] have been developed to improve its performance. Nevertheless, the practical implementation of 1D SnO_2 nanomaterials is hampered by its low initial coulombic efficiency, owing to Li_2O formation, and the poor capacity retention because of the pulverization which occurs during extended charge–discharge cycling.

Many feasible strategies have been applied to improve the Li^+ storage capacity and cyclability of one-dimensional SnO_2 nanomaterials, including the introduction of some dispersed materials with little volume variation during the charge–discharge cycling, such as TiO_2,[8] and the use of a buffer matrix, such as carbon.[6,18,19] Both strategies can overcome the problems caused by volume expansion during cycling, because of the "buffering" (cushioning effect) and "mechanical support" functions. Up to now, however, only a few one-dimensional TiO_2/SnO_2/carbon nanomaterials, such as TiO_2/SnO_2/carbon nanotubes (CNTs)[20] and TiO_2(B)@SnO_2/carbon hybrid nanowires,[21] have been reported for use as anode materials for lithium ion batteries. Thus, there are still some challenges in the synthesis of 1D TiO_2/SnO_2/carbon hybrid nanomaterials, especially when they are to be produced by simple methods. Electrospinning is one such simple method to form continuous one-dimensional nanofibers under the electrostatic force of the charges on the surface of a liquid droplet in a sufficiently high electric field, which is applied between the capillary nozzle and the metal collector.[12,13,22,23]

Herein, this paper presents a relatively simple and low-cost approach for preparing TiO_2/SnO_2/carbon hybrid nanofibers by a combination of electrospinning and subsequent thermal treatment. The as-prepared TiO_2/SnO_2/carbon nanofibers have several unique advantages, such as high porosity, three-dimensional architecture and a large surface-to-volume ratio. The TiO_2 in the TiO_2/SnO_2/carbon nanofibers not only works as a mechanical support, which effectively buffers the volume changes of tin during lithium ion intercalation–de-intercalation, but also protects the tin crystals from agglomeration and contributes to the capacity within a certain voltage range. The carbon matrix can also buffer the volume change and prevent the agglomeration of tin during the charge–discharge cycling. In addition, the good conductivity of carbon in the hybrid

[a]National & Local United Engineering Laboratory of Flat Panel Display Technology, Fuzhou University, Fuzhou 350002, P. R. China. E-mail: yangzunxian@hotmail.com
[b]Institute for Superconducting & Electronic Materials, University of Wollongong, NSW 2522, Australia. E-mail: zguo@uow.edu.au; Fax: +61 2 4221 5731; Tel: +61 2 4221 5225
[c]School of Mechanical, Materials & Mechatronics Engineering, University of Wollongong, NSW 2522, Australia
[d]Department of Materials Science, Fudan University, Shanghai 200433, P. R. China. E-mail: yuxuebin@fudan.edu.cn
[e]School of Computing, Engineering and Mathematics, University of Western Sydney, NSW 2751, Australia

† Electronic supplementary information (ESI) available. See DOI: 10.1039/c3ta11751k

composite can improve the electrical conductivity of the composite and further enhance the electrochemical performance. The as-prepared TiO_2/SnO_2/carbon nanofibers have been investigated in a preliminary manner for potential use as anode materials for lithium ion batteries, and exhibit excellent cycling stability.

2 Experimental

2.1 Synthesis of TiO_2/SnO_2/carbon and TiO_2/SnO_2 composite nanofibers

The procedures for preparing the electrospinning solution are similar to those in previously reported work.[12,13,22–25] Briefly, 0.7 g polyacrylonitrile (PAN, $M_W = 150\,000$, Aldrich) was dissolved in 5.6 g *N*,*N*-dimethylformamide (DMF, 99.8%, Aldrich) at 80 °C with vigorous stirring for 2 h (solution no. 1), and then, 1.0 g titanium(IV) isopropoxide (97%, Aldrich) was mixed with 2.4 g anhydrous ethanol and 3.1 g acetic acid (solution no. 2). Afterwards, solution no. 2 was added dropwise to solution no. 1 at 80 °C with vigorous stirring. Subsequently, different contents of tin(II) 2-ethylhexanoate (95%, Aldrich) were further added dropwise to the above mixed solution at 80 °C with vigorous stirring (see Table 1). The mixed solution was then stirred at room temperature for 3 h. The polymer solution was transferred into a 10 mL syringe with a capillary tip (0.8 mm diameter). For spinning, the setup was similar to that described previously.[12,13,22,26] Typically, the collector was placed 9.5 cm from the spinneret to collect the nanofibers. A high voltage of 13.3 kV was applied between the spinneret and the collector by a direct-current power supply (DW-P303-5ACCD, Tianjin Dongwen High Voltage Power Supply Co., China). The solution was pushed out of the spinneret by a syringe pump (TS2-60, Baoding Lange Constant Flux Pump Co., China) at a rate of 0.3 mL h^{-1}. The collector was kept at 180 °C during the electrospinning process to evaporate the solvent. After spinning for more than twenty hours, the nanofiber films were easily peeled off. The electrospun nanofibers were slowly decarbonized at 500 °C for 2 h in an air environment (heating rate less than 1 °C min^{-1}) or carbonized at 500 °C for 2 h in an argon atmosphere (heating rate less than 1 °C min^{-1}). Finally, a white film (TiO_2/SnO_2 nanofibers) and a black film (TiO_2/SnO_2/carbon nanofibers) were obtained, respectively.

2.2 Materials characterization

Thermogravimetric analysis (TGA) of the as-prepared TiO_2/SnO_2/carbon hybrid nanofibers in samples **TSC1**, **TSC2**, and **TSC3** (see Table 1 for sample labels) was carried out with a TGA/DSC1-type instrument (METTLER TOLEDO, Switzerland) at a heating rate of 10 °C min^{-1} from 25 to 1000 °C in air. The composition and crystal structure of the as-prepared nanofibers were obtained by X-ray diffraction (XRD) analysis (MMA, GBC, Australia). The morphology of the as-synthesized nanofibers was evaluated using field emission scanning electron microscopy (FE-SEM, JEOL 7500FA, JEOL, Tokyo, Japan) and transmission electron microscopy (TEM, JEOL 2011F, JEOL, Tokyo, Japan). Energy dispersive X-ray spectroscopy (EDX, JEOL 7500FA) was used to confirm the carbon, SnO_2 and TiO_2 contents. X-ray photoelectron spectroscopy (XPS) experiments were carried out on a VG Scientific ESCALAB 220IXL instrument, using aluminum Kα X-ray radiation.

2.3 Electrochemical characterization

The electrochemical properties were measured on electrodes prepared by compressing a mixture of the as-prepared TiO_2/SnO_2/carbon or TiO_2/SnO_2 hybrid nanofibers, carbon black (Super P, MMM, Belgium), and poly(vinyl difluoride) (PVDF) binder in a weight ratio of 80 : 10 : 10, and pasting the mixture on copper foil. Pure lithium metal foil was used for the counter and reference electrodes. The electrolyte was $LiPF_6$ (1 M) in a mixture of ethylene carbonate (EC) and dimethyl carbonate (DMC) (1 : 1 v/v; MERCK KgaA, Germany). The coin cells were assembled in a high-purity argon-filled glove box (Mbraun, Unilab, Germany). A LAND-CT2001A instrument was used with a charge–discharge current density of 30 mA g^{-1} to measure the electrochemical capacity of the electrodes at room temperature by the galvanostatic method. The rate capability tests of the electrodes were then carried out systematically. The cut-off potentials for charge and discharge were set at 3.0 and 0.01 V *versus* Li^+/Li, respectively. Cyclic voltammetry (CV) was performed on a PARSTAT@2273 electrochemical workstation.

3 Results and discussion

Fig. 1 presents the powder X-ray diffraction (XRD) patterns of the as prepared TiO_2/SnO_2/carbon and TiO_2/SnO_2 hybrid nanofibers. After the heat treatment in argon, there are no sharp

Table 1 Composite precursors and heat treatment environment for the as-synthesized composite nanowires

	Composition of precursors for samples					
Sample number	Polyacrylonitrile (g)	Tin(II) 2-ethylhexanoate (g)	Titanium(IV) isopropoxide (g)	Heat treatment temperature (°C)	Heat treatment environment	As-synthesized composite nanowires
TSC1	0.70	0.14	1.0	500	Argon	TiO_2/SnO_2/carbon
TS1	0.70	0.14	1.0	500	Air	TiO_2/SnO_2
TSC2	0.70	0.264	1.0	500	Argon	TiO_2/SnO_2/carbon
TS2	0.70	0.264	1.0	500	Air	TiO_2/SnO_2
TSC3	0.70	0.356	1.0	500	Argon	TiO_2/SnO_2/carbon
TS3	0.70	0.356	1.0	500	Air	TiO_2/SnO_2

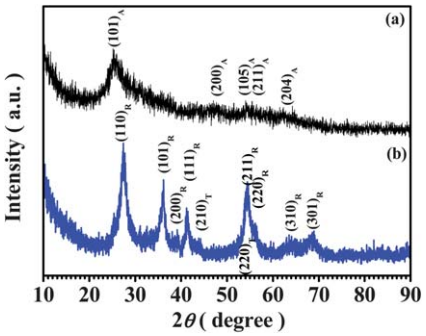

Fig. 1 X-ray diffraction patterns of the as-prepared **TS1** and **TSC1** samples: (a) TiO_2/SnO_2/carbon hybrid nanofibers (**TSC1**) consisting of mainly anatase with the tetragonal structure (JCPDS 21-1272); (b) TiO_2/SnO_2 hybrid nanofibers (**TS1**) consisting of rutile with the tetragonal structure (JCPDS 76-0649) and minor cassiterite SnO_2 with the tetragonal structure (JCPDS 76-0450), as indexed in the patterns. The subscripts "A", "R", and "T" represent the anatase, rutile and tin oxide peaks in the samples, respectively.

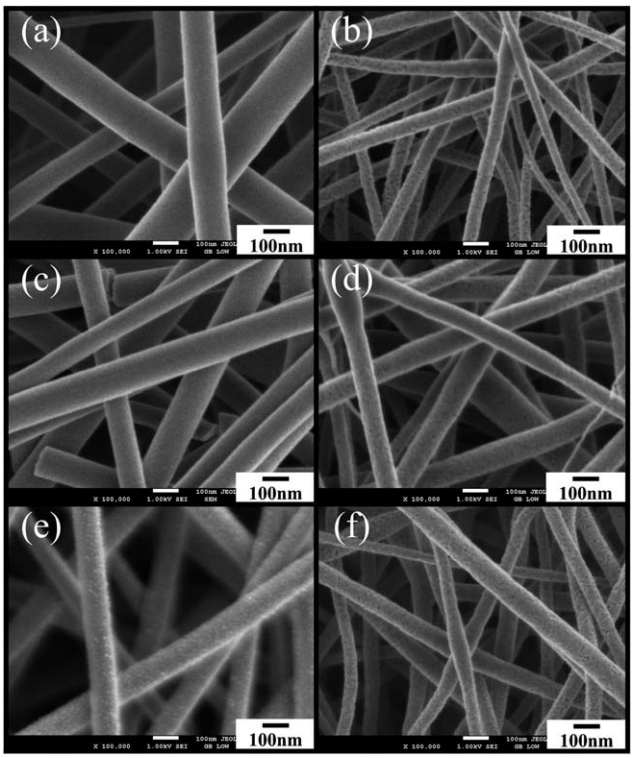

Fig. 2 FE-SEM images of the as-synthesized hybrid nanofibers at high magnification: (a) **TSC1**, (b) **TS1**, (c) **TSC2**, (d) **TS2**, (e) **TSC3** and (f) **TS3**. (Gold nanoparticles with grain sizes of ~5 to 10 nm were evaporated on the surfaces of the **TS1**, **TS2** and **TS3** samples to reduce electrostatic charging during the SEM imaging.)

characteristic peaks in the X-ray diffraction pattern, possibly because of the poor crystallinity of the TiO_2/SnO_2/carbon hybrid nanofibers produced *via* heat treatment at low temperature, as well as the interference of the high carbon content in the hybrid nanofibers. The anatase TiO_2 (JCPDS 21-1272) in the TiO_2/SnO_2/carbon hybrid nanofibers can still be detected (see Fig. 1(a)). When the sample was heat-treated in air, however, the titanium–tin/PAN nanofiber composite was transformed into TiO_2/SnO_2 nanofibers, in which the main phase, rutile TiO_2 with the tetragonal structure (JCPDS 76-0649) (see Fig. 1(b)), can be detected, while some other small peaks can be indexed to SnO_2 with the tetragonal structure (JCPDS 76-0450). This is possibly due to the nanocrystalline nature of SnO_2 in the TiO_2/SnO_2 nanofibers. Therefore, the post-heat treatment of the as-spun titanium–tin/PAN composite in an argon atmosphere facilitates the formation of anatase phase TiO_2, while post-heat treatment in air promotes the formation of rutile TiO_2.

The field emission scanning electron microscopy (FE-SEM) images (see Fig. 2 and S2†) show the morphologies of the as-synthesized TiO_2/SnO_2/carbon and TiO_2/SnO_2 hybrid nanofibers. Fig. 2(a), (c) and (e) and S2(a), (c) and (e)† display the morphology of the TiO_2/SnO_2/carbon nanofiber samples (**TSC1**, **TSC2**, and **TSC3**) synthesized by the electrospinning process and subsequent carbonization in an inert atmosphere, while Fig. 2(b), (d) and (f) and S2(b), (d) and (f)† show those of the TiO_2/SnO_2 hybrid nanofiber samples (**TS1**, **TS2** and **TS3**) obtained after heat treatment in air. The TiO_2/SnO_2/carbon nanofibers (**TSC1**, **TSC2** and **TSC3**) have diameters of 80–150 nm and extend to a few micrometers, and even to a few millimeters in length (see Fig. 2 and S2†), while the TiO_2/SnO_2 nanofibers (**TS1**, **TS2** and **TS3**) have diameters of 50–100 nm, much thinner than those of the TiO_2/SnO_2/carbon nanofiber samples, which is can be partly attributed to the removal of the carbon matrix from the hybrid nanofibers under the heat treatment in air. Additionally, the TiO_2/SnO_2 particle size in the TiO_2/SnO_2/carbon nanofibers is smaller than in the TiO_2/SnO_2 nanofibers, which is in good agreement with the XRD patterns and may be due to the confinement effect of the carbon matrix during fabrication. Obviously, the TiO_2/SnO_2/carbon nanofibers in **TSC3** have more nanoparticles or nanocrystals attached around the nanofibers than in **TSC1** and **TSC2**, which is due to the relatively higher ratio of TiO_2/SnO_2 to carbon from the higher concentration of the tin(II) 2-ethylhexanoate precursor solution used in the electrospinning process for the **TSC3** sample. Furthermore, there are many nanopores among the TiO_2/SnO_2 nanoparticles in all of the nanofiber samples, which can be attributed to the pyrolysis of PAN in the hybrid nanofibers and will be of great advantage to electrolyte access, and furthermore, to the electrochemical performance. Some TiO_2/SnO_2/carbon nanofibers and TiO_2/SnO_2 nanofibers (see Fig. 2 and S2† and its insets) have aggregated to form larger pores or gaps in the electrode materials, which make them more favorable for electrolyte diffusion.

The transmission electron microscopy (TEM) images, combined with the selected area electron diffraction (SAED) patterns of **TSC1** and **TS1**, presented in Fig. 3 and S3,† indicate that the synthesized nanofibers consist of many nanocrystals with average particle sizes of about 5 nm for **TSC1** and 10 nm for **TS1**, respectively. Fig. 3(a and b) display TEM bright-field images of the **TSC1** sample, revealing that each TiO_2/SnO_2/carbon nanofiber actually consists of many TiO_2/SnO_2 nanocrystals. The obvious diffraction ring of the SAED pattern, which can be indexed as the (101) plane of anatase TiO_2 (see Fig. 3(b) and its inset), indicates the polycrystalline nature of the

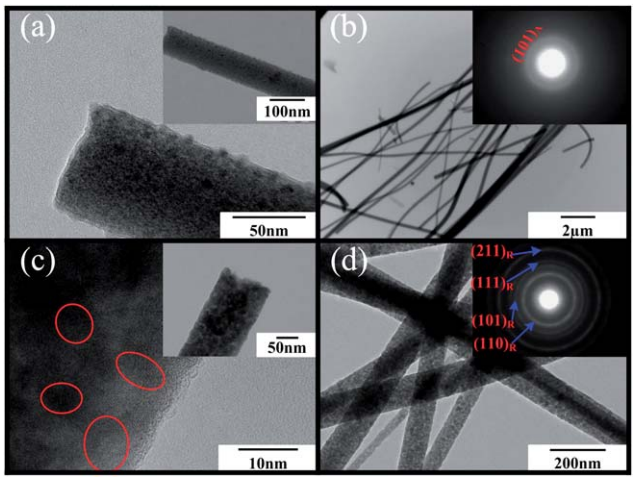

Fig. 3 (a) High resolution TEM (HRTEM) image and lower-magnification TEM image (inset) of a single **TSC1** nanofiber, (b) low-magnification TEM image and SAED pattern (inset) of the **TSC1** hybrid nanofibers, (c) HRTEM image and lower-magnification TEM image (inset) of a single **TS1** nanofiber and (d) low-magnification TEM image and SAED pattern (inset) of the **TS1** nanofibers. (In these TEM patterns, the subscripts "A" and "R" represent anatase TiO_2 and rutile TiO_2, respectively.) The areas in the red ellipses in (c) belong to individual single crystals.

TiO_2/SnO_2/carbon nanofibers. Fig. 3(c and d) and S3(a and b)† show that the **TS1** TiO_2/SnO_2 hybrid nanofiber sample, derived from the as-electrospun titanium–tin composite/PAN hybrid nanofibers after heat-treatment in an air atmosphere, consists of many TiO_2/SnO_2 nanocrystals (see Fig. S3(b)† and 3(c)). Similarly, due to the polycrystalline nature of the TiO_2/SnO_2 hybrid nanofibers, the four most intense diffraction rings from inside to outside can be indexed as the (110), (101), (111) and (211) planes of rutile TiO_2, respectively (see Fig. 3(d) and its inset). Furthermore, as shown in Fig. S3(b),† after calcination in air, the **TS1** TiO_2/SnO_2 nanofibers display the rutile structure with an interplanar spacing of approximately 0.32 nm between the neighboring (110) planes of tetragonal TiO_2, but with crystal sizes of ~10 nm, larger than for the **TSC1** TiO_2/SnO_2/carbon nanofibers. Fig. S4 reveals chemical information on the as-prepared TiO_2/SnO_2 nanofibers and TiO_2/SnO_2/carbon nanofibers *via* energy dispersive X-ray (EDX) spectroscopy. The **TS1**, **TS2** and **TS3** composite nanofibers mainly include the elements Ti, O and Sn, while there are some extra carbon signals from the **TSC1**, **TSC2** and **TSC3** samples, as well as the above-mentioned elements, which is different from the TEM and XRD results where almost no SnO_2 signal could be detected, owing to the nanocrystalline nature of SnO_2 in these nanofibers. As shown in the insets of Fig. S4(a), (c) and (e),† the heat treatment at 500 °C for 2 h in argon leads to composite nanofibers with a carbon content of 32.61% in **TSC1**, 25.04% in **TSC2** and 28.37% in **TSC3**. The abnormal increase in the carbon content in **TSC3** is possibly due to an amount of Sn uncovered by the carbon matrix (Fig. 2(e)) and further evaporated during the heat treatment process (see Fig. S4(e)† and its inset).

X-ray photoelectron spectroscopy (XPS) analysis was performed from 0 to 1100 eV for **TSC1**, **TS1**, **TSC3** and **TS3**, respectively (see Fig. 4 and S5†). Obvious Ti 2p, Sn 3d, O 1s and C 1s peaks were detected, and their high-resolution spectra are shown in Fig. 4 (**TSC1** and **TS1**) and Fig. S5† (**TSC3** and **TS3**). In the Ti 2p spectrum (Fig. 4(a)) of **TSC1**, there are two symmetrical peaks with binding energies (BEs) of 459.2 eV and 464.57 eV, which can be attributed to Ti $2p^{3/2}$ and Ti $2p^{1/2}$, respectively. The separation between these two peaks is 5.37 eV, slightly smaller than the energy splitting reported for TiO_2 (ref. 21 and 27–30) and that of **TS1**, with two symmetrical peaks at 458.89 eV and 464.55 eV (see Fig. 4(b)). The higher binding energies of Ti $2p^{3/2}$ and Ti $2p^{1/2}$, and the slightly thinner BE splitting for **TSC1**, can possibly be ascribed to the synergetic effect of the different morphology of TiO_2 in **TSC1** and the presence of Ti–O–C[31] bonds at the TiO_2/SnO_2/carbon interface, which has been further verified by the Ti 2p spectra (Fig. S5(a and b)†) for **TSC3** and **TS3**. Similar phenomena relating to the Sn $3d^{5/2}$ and Sn $3d^{3/2}$ peaks in **TSC1** and **TS1** have also been observed, as shown in Fig. 4(c and d). The two symmetrical peaks with BEs at 487.09 eV and 495.51 eV (Fig. 4(c)) can be assigned to Sn $3d^{5/2}$

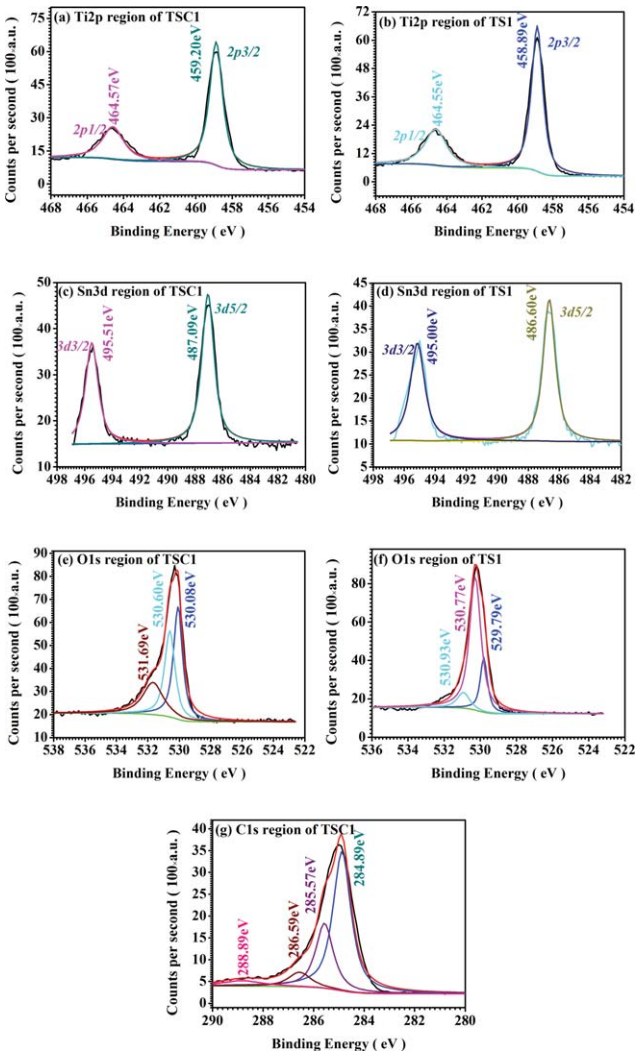

Fig. 4 XPS high-resolution spectra with curve fitting of the (a) Ti 2p region of **TSC1**, (b) Ti 2p region of **TS1**, (c) Sn 3d region of **TSC1**, (d) Sn 3d region of **TS1**, (e) O 1s region of **TSC1**, (f) O 1s region of **TS1** and (g) C1s region of **TSC1**.

and Sn $3d^{3/2}$ in **TSC1**, respectively, while the two peaks at 486.60 eV and 495.50 eV in **TS1** (Fig. 4(d)) are associated with their counterparts in **TSC1**. The higher binding energies for Sn $3d^{5/2}$ and Sn $3d^{3/2}$, but the thinner BE splitting for **TSC1**, are also possibly attributable to the formation of Sn–O–C[12,13,31] bonds. This phenomenon has also been detected in the Sn 3d spectra for the **TSC3** and **TS3** samples (see Fig. S5(c and d)†). As demonstrated in Fig. 4(e and f) and S5(e and f),† the O 1s BE peaks at 530.08 eV in **TSC1**, 529.79 eV in **TS1**, 530.10 eV in **TSC3** and 529.80 eV in **TS3** could result from the TiO_2 or Ti–O–C,[31,32] while the peaks at 530.60 eV in **TSC1**, 530.77 eV in **TS1**, 530.67 eV in **TSC3** and 530.32 eV in **TS3** may be attributable to the SnO_2 (ref. 31) and Sn–O–C formation.[13] The higher O 1s peaks at 531.69 eV in **TSC1**, 530.93 eV in **TS1**, 532.09 eV in **TSC3** and 531.17 eV in **TS3** possibly originate from C–O bonds[13,31] and from OH^- radicals, adsorbed oxygen or adsorbed H_2O.[31] Fig. 4(g) and S5(g),† containing high-resolution spectra of the C 1s region of **TSC1** and **TSC3**, have been fitted to four peaks. The large peaks at 284.89 eV for **TSC1** and 284.81 eV for **TSC3** are possibly attributable to graphitic carbon with a polyaromatic layered structure,[31] while the peaks at 285.57 eV for **TSC1** and 285.42 eV for **TSC3** could be assigned to disordered carbon. The higher binding energy peaks at 286.59 eV for **TSC1** and 286.35 eV for **TSC3** are probably attributable to Ti–O–C or Sn–O–C in the composites, respectively, which is in good agreement with the as-analyzed results of Ti 2p and Sn 3d. The binding energy peaks at 288.89 eV for **TSC1** and 289.10 eV for **TSC3** are possibly attributable to the presence of some hydroxyl or carboxyl groups.[31] Thus, the combination of the XRD, FE-SEM, TEM, EDX and XPS results confirms that the as-synthesized TiO_2/SnO_2/carbon and TiO_2/SnO_2 hybrid nanofiber composites consist of polycrystalline anatase TiO_2/SnO_2 and of polycrystalline rutile TiO_2/SnO_2, respectively, where each particle is a small crystal, mainly owing to the low diffusion capability of TiO_2/SnO_2 in those nanofibers at the relatively low pyrolysis temperature.[33] Additionally, the nanosized TiO_2/SnO_2 crystals in the TiO_2/SnO_2/carbon nanofibers are uniformly dispersed into and encapsulated in the carbon matrix, while the carbon component exists as a porous carbon matrix with many holes/voids, mainly left from the PAN pyrolysis. Relatively large pores also formed between cross-linked nanofibers. The TiO_2/SnO_2/carbon nanofibers consisting of TiO_2/SnO_2 nanocrystals and porous carbon should exhibit unique advantages in lithium battery applications, such as high conductivity due to the abundant porous carbon matrix, and improved Li^+ and electrolyte transport in the hybrid nanofibers because of their high porosity. These factors enhanced the electrochemical performance of the electrode as compared with the TiO_2/SnO_2 nanofiber electrode without carbon.

The electrochemical performance of both the TiO_2/SnO_2/carbon nanofiber electrodes (**TSC1**, **TSC2** and **TSC3**) and the TiO_2/SnO_2 nanofiber electrodes (**TS1**, **TS2** and **TS3**) were investigated systematically using 2032 coin cells, in which lithium foil served as both the counter and reference electrodes (see Fig. 5(a–c) and Fig. S6†). Cyclic voltammograms (CVs) of the TiO_2/SnO_2/carbon nanofiber electrode (**TSC3**) from the first to the fifth cycle at a scan rate of 0.1 mV s^{-1} were obtained and are presented in Fig. 5(a). For comparison purposes, the CV curves of the TiO_2/SnO_2 nanofiber electrode (**TS2**) in the voltage range of 0.01–3.0 V are shown in Fig. S6.† The curves of the initial cycle for both the TiO_2/SnO_2/carbon nanofiber and the TiO_2/SnO_2 nanofiber electrodes are different from those in the following cycles, mainly because of the gradual disappearance of some high CV peaks, which is possibly due to the gradual formation of an inactive solid/electrolyte interphase (SEI) on the surface of the active materials. From the third cycle onwards, the CV curves of these electrodes become stable, indicating their good cycling performance (see Fig. 5(a) and Fig. S6†). In the first cycle, the cathodic/anodic peak pairs at 0.018 V and 0.168 V (Fig. 5(a)) correspond to the lithium insertion–extraction in carbon, while the peaks at around 0.36 V and 0.54 V (Fig. 5(a)) are mainly attributable to the formation of various Li_xSn phases, such as Li_2Sn_5, LiSn, Li_7Sn_3, Li_5Sn_2, $Li_{13}Sn_5$, Li_7Sn_2 and $Li_{22}Sn_5$, during the charge–discharge process.[34] The obvious peak pair at 1.022 V and 1.19 V (see Fig. 5(a)) results from Li_2O formation and electrolyte decomposition,[7] which is partly responsible for the large irreversible capacity in the first cycle. Additionally, another small cathodic/anodic peak pair at 1.63 V and 1.90 V in the first cycle (Fig. 5(a)) can be ascribed to the lithium ion insertion into/extraction out of anatase TiO_2,[35] while the cathodic/anodic peak pair at 1.561 V and 1.876 V in the first cycle (Fig. S6†) is attributable to the lithium ion insertion into/extraction out of rutile TiO_2.[36] The TiO_2 in the composite not only alleviates the pulverization and drastic volume variation of the SnO_2, but also contributes to the electrochemically active Sn/Sn–Ti–O bilayer[34] in the hybrid nanofiber, which acts as a stable membrane for the Li-ion insertion and extraction processes and will thus facilitate the reversible Li-ion intercalation–de-intercalation. There are unknown peaks at 2.35 V (Fig. 5(a)) and 2.312 V (Fig. S6†) in the first cycle, however, which disappear gradually in the next few cycles. The reason or the corresponding reaction for these peaks is still unclear. Further work may be conducted in order to clarify this in the future.

The anode performance of the composite electrodes was tested in the voltage range of 0.01–3.0 V (*versus* Li/Li^+) at a current density of 30 mA g^{-1} for 100 cycles. Fig. 5(b) reveals the voltage profiles of the **TSC1**, **TS1**, **TSC2**, **TS2**, **TSC3** and **TS3** electrodes in their first cycles. The first discharge and charge capacities of **TSC1** are 837.47 and 590.41 mA h g^{-1}, respectively, indicating a coulombic efficiency of ~70.49%, whereas the first discharge and charge capacities respectively of **TS1**, **TSC2**, **TS2**, **TSC3** and **TS3** are 568.07 and 350.80 mA h g^{-1}, 1009.92 and 616.46 mA h g^{-1}, 587.25 and 388.74 mA h g^{-1}, 834.11 and 451.60 mA h g^{-1}, and 687.0 and 471.13 mA h g^{-1}, with coulombic efficiencies of 61.75%, 61.03%, 66.19%, 54.14% and 68.57%, respectively. Although the coulombic efficiencies of the samples are not high, the coulombic efficiency of the TiO_2/SnO_2/carbon electrodes is higher compared to SnO_2/carbon composite electrodes fabricated by the same technique (Fig. S7†). Fig. 5(c) displays the cycling performance of the **TSC1**, **TS1**, **TSC2**, **TS2**, **TSC3** and **TS3** electrodes from the first cycle to the 100^{th} cycle at a current density of 30 mA g^{-1}. The **TSC1** electrode exhibits good cycling performance and a reversible specific capacity of 438.9 mA h g^{-1} up to 100 cycles, with a high

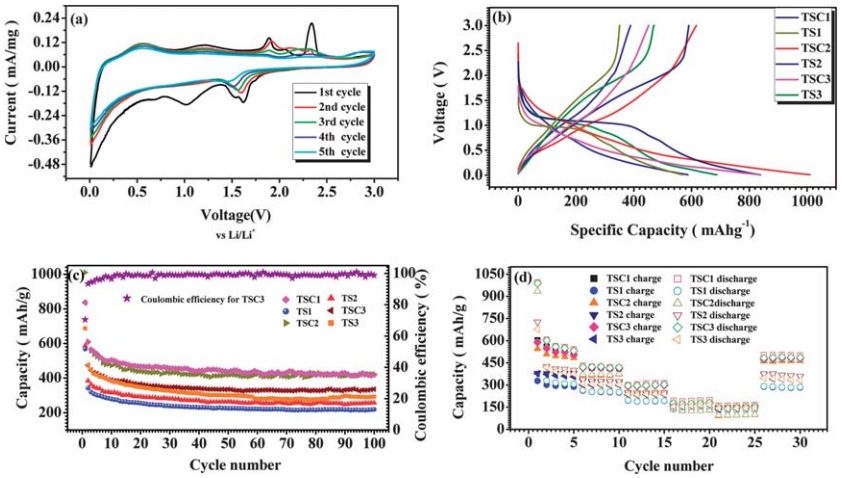

Fig. 5 Electrochemical performance of the as-synthesized hybrid nanowire electrodes: (a) Cyclic voltammograms of the **TSC3** electrode from the first cycle to the fifth cycle at a scan rate of 0.1 mV s^{-1} in the voltage range of 0.01–3.0 V. (b) Galvanostatic voltage profiles of the **TSC1**, **TS1**, **TSC2**, **TS2**, **TSC3** and **TS3** electrodes for the first cycle at a cycling rate of 30 mA g^{-1} in the voltage range of 0.01–3.0 V *vs.* Li^+/Li. (c) Capacity–cycle number curves of the **TSC1**, **TS1**, **TSC2**, **TS2**, **TSC3** and **TS3** electrodes from the first cycle to the 100th cycle for the hybrid nanofibers at a current density of 30 mA g^{-1}, cycled between 0.01 and 3.0 V *vs.* Li^+/Li. (d) Charge and discharge capacity for the **TSC1**, **TS1**, **TSC2**, **TS2**, **TSC3** and **TS3** electrodes at different currents: 30 mA g^{-1}, 100 mA g^{-1}, 500 mA g^{-1}, 1000 mA g^{-1} and 2000 mA g^{-1}. (**TSC** and **TS** are abbreviations of TiO_2/SnO_2/carbon and TiO_2/SnO_2, respectively.)

coulombic efficiency of nearly 100%. The higher reversible capacity of **TSC1** compared to that of **TS1** is attributable to the special structure of **TSC1**, *i.e.*, the SnO_2 nanocrystals supported by TiO_2 and further encapsulated in the carbon matrix. The **TSC2** and **TSC3** samples exhibit very good cycling performance, as compared to the TiO_2/SnO_2 nanofibers. The **TSC2** and **TSC3** electrodes deliver reversible capacities of 442.8 mA h g^{-1} and 348.2 mA h g^{-1} for 100 cycles, respectively. The higher specific capacity of **TSC2** but lower specific capacity of **TSC3** as compared with **TSC1** probably relates to the synergetic action between the content of SnO_2/carbon and the dispersion and encapsulation of carbon and TiO_2 in the composite. The former factor is favorable for improving the capacity of the composite, while the latter factor will be of great advantage to the cycling performance. It should be noted that the cycling performance of all of the TSC (TiO_2/SnO_2/C) and TS (TiO_2/SnO_2) samples is significantly improved compared to those of SnO_2/carbon nanofibers,[12,37] SnO_2 nanofibers[22] and TiO_2/carbon nanofibers[23,38] fabricated by the same technique (Fig. S7†), indicating that the presence of TiO_2 in the composite contributes significantly to the structural stability of the electrodes, verifying its mechanical supporting effect. Fig. 5(d) shows the rate performance of the **TSC1**, **TS1**, **TSC2**, **TS2**, **TSC3** and **TS3** electrodes at different current densities of 30, 100, 500, 1000 and 2000 mA g^{-1}. It is worth noting that the **TSC1** electrode exhibits the best rate capability, with a capacity of 541.08 mA h g^{-1} at a current density of 30 mA g^{-1} after 5 cycles. This value decreases to 415 mA h g^{-1} at 100 mA g^{-1}, 313.9 mA h g^{-1} at 500 mA g^{-1}, 198.36 mA h g^{-1} at 1000 mA g^{-1} and 165.0 mA h g^{-1} at 2000 mA g^{-1}, and finally recovers to 500.31 mA h g^{-1} when the current density is increased to 30 mA g^{-1}, which is probably attributable to the high conductivity of **TSC1** due to its higher content of porous carbon as compared with the other samples. The improved coulombic efficiency and reversible cycling performance of the **TSC** samples are mainly attributable to the special structure of the one-dimensional porous nanofibers, in which SnO_2 nanocrystals are dispersed among TiO_2 nanocrystals and further encapsulated in a porous carbon matrix, which provides the "buffering" (cushioning effect) and "mechanical support" functions during the charge–discharge cycling for the tin nanoparticles, as well as the high conductivity, owing to the high content of carbon in these composites (see Fig. S1†). Electrochemical impedance spectroscopy (EIS) measurements were carried out to further investigate the electrochemical performance of the TiO_2/SnO_2/carbon hybrid nanofibers with respect to the TiO_2/SnO_2 electrodes, and were recorded from 0.1 Hz to 100 MHz. The equivalent electrical circuit models of these systems are shown in Fig. S8,† and the fitted impedance parameters are listed in Table S1.† As shown in Table S1,† the charge transfer resistance, R_{ct}, which is 243.1 Ω for the **TS1** electrode and 38.39 Ω for the **TSC1** electrode, has been effectively reduced after coating the carbon matrix on the TiO_2/SnO_2 nanoparticles. Due to the carbon matrix layers, both the electronic conductivity of the electrode materials and the stability of the SEI films are greatly enhanced,[39,40] which results in a significant improvement in the electrochemical performance. The TiO_2/SnO_2/carbon hybrid nanofibers with high reversible capacity and excellent cycling stability are one of the most promising anode materials for LIBs.

To clearly explain the charge transfer behavior in the TiO_2/SnO_2/carbon nanofibers (**TSC1**, **TSC2** and **TSC3**) and the TiO_2/SnO_2 nanofibers (**TS1**, **TS2** and **TS3**) during the charge–discharge processes, charge transfer models for these samples are proposed in Fig. S9.† Nanosized TiO_2/SnO_2 crystals were uniformly encapsulated in the porous carbon matrix to form cross-linked TiO_2/SnO_2/carbon nanofibers, which have a large amount of nanopores due to the pyrolysis of PAN during the heat treatment, as well as micropores formed between the cross-linked TiO_2/SnO_2/carbon nanofibers. The electrons can rapidly transfer to the

SnO_2 and TiO_2 nanocrystals *via* the highly conductive carbon matrix network,[41,42] while the lithium ions can effectively diffuse to the SnO_2 and TiO_2 nanocrystals through the micropores and nanopores. The carbon matrix and TiO_2, which has a small volume expansion ratio (3%) upon the intercalation–extraction of Li ions, also accommodate the enormous volume change of the SnO_2 nanocrystals, protect the SnO_2 nanocrystals from aggregation and restrict the growth of the SEI layer. All of these functions lead to the long-term cycling stability of the TiO_2/SnO_2/carbon nanofiber electrodes. As for the TiO_2/SnO_2 nanofibers, although there are also many micropores between the cross-linked TiO_2/SnO_2 nanofibers, the conductivity of the TiO_2/SnO_2 nanofibers is lower compared to that of the TiO_2/SnO_2/carbon samples, leading to a much lower discharge–charge capacity. Therefore, it is both the nanoscale TiO_2/SnO_2 crystals and the highly porous carbon matrix in the TiO_2/SnO_2/carbon nanofibers which ensure a good electrode–electrolyte contact, good electronic conductivity, good mechanical support and short lithium ion diffusion pathways during the discharge–charge cycling, and thus make a great contribution to the enhanced electrochemical performance of the electrodes.

4 Conclusions

In summary, very large area, uniform TiO_2/SnO_2/carbon nanofibers and TiO_2/SnO_2 nanofibers have been prepared by the thermal pyrolysis and oxidation of titanium–tin/PAN nanoweb composites in argon or in air, respectively. The as-prepared TiO_2/SnO_2/carbon nanofibers exhibit excellent properties in terms of cycling performance and rate capability as an anode material for lithium ion batteries, benefiting from the nanosized SnO_2/TiO_2 particles, the highly conductive carbon matrix, the highly porous network structure and the mechanical support effect of the TiO_2. The TiO_2/SnO_2/carbon nanofiber electrodes exhibit excellent cycling performance with a reversible capacity of 442.8 mA h g^{-1} for 100 cycles and a high coulombic efficiency of nearly 100%. The synthesis technique, *i.e.* the desirable confinement of SnO_2 and TiO_2 nanocrystals in nanoporous carbon networks, could be a useful way to boost the electrochemical performance of other nanomaterials.

Acknowledgements

Part of the work was funded by the Australian Research Council (ARC) through a Discovery project (DP1094261), the Natural Science Foundation Program of Fujian Province (2010J01332), the Science Development Foundation of Fuzhou University (2012-XQ-40) and the Foundation Program of the Ministry of Education for Returned Exchange Personnel (LXKQ201101). The authors would also like to thank Dr Tania Silver at the University of Wollongong for critical reading of the manuscript and Mr Darren Attard for his great contribution.

References

1 N. Du, H. Zhang, X. Ma and D. Yang, *Chem. Commun.*, 2008, 6182–6184.
2 S. Gubbala, V. Chakrapani, V. Kumar and M. K. Sunkara, *Adv. Funct. Mater.*, 2008, **18**, 2411–2418.
3 Z. Y. Liu, D. D. L. Sun, P. Guo and J. O. Leckie, *Nano Lett.*, 2007, **7**, 1081–1085.
4 Y. S. Zhang, K. Yu, G. D. Li, D. Y. Peng, Q. X. Zhang, F. Xu, W. Bai, S. X. Ouyang and Z. Q. Zhu, *Mater. Lett.*, 2006, **60**, 3109–3112.
5 R. K. Selvan, I. Perelshtein, N. Perkas and A. Gedanken, *J. Phys. Chem. C*, 2008, **112**, 1825–1830.
6 Z. Wen, Q. Wang, Q. Zhang and J. Li, *Adv. Funct. Mater.*, 2007, **17**, 2772–2778.
7 X. W. Lou, C. M. Li and L. A. Archer, *Adv. Mater.*, 2009, **21**, 2536–2539.
8 J. S. Chen, D. Y. Luan, C. M. Li, F. Y. C. Boey, S. Z. Qiao and X. W. Lou, *Chem. Commun.*, 2010, **46**, 8252–8254.
9 R. Demir-Cakan, Y.-S. Hu, M. Antonietti, J. Maier and M.-M. Titirici, *Chem. Mater.*, 2008, **20**, 1227–1229.
10 C. M. Park, W. S. Chang, H. Jung, J. H. Kim and H. J. Sohn, *Electrochem. Commun.*, 2009, **11**, 2165–2168.
11 H. K. Wang, F. Fu, F. H. Zhang, H. E. Wang, S. V. Kershaw, J. Q. Xu, S. G. Sun and A. L. Rogach, *J. Mater. Chem.*, 2012, **22**, 2140–2148.
12 Z. X. Yang, G. D. Du, Z. P. Guo, X. B. Yu, Z. X. Chen, P. Zhang, G. N. Chen and H. K. Liu, *J. Mater. Res.*, 2010, **25**, 1516–1524.
13 R. S. Ningthoujam, R. Mishra, D. Das, G. K. Dey and S. K. Kulshreshtha, *J. Nanosci. Nanotechnol.*, 2008, **8**, 4176–4180.
14 H. Y. Mi, Y. L. Xu, W. Shi, H. D. Yoo, S. J. Park, Y. W. Park and S. M. Oh, *J. Mater. Chem.*, 2011, **21**, 19302–19309.
15 M. S. Park, Y. M. Kang, S. X. Dou and H. K. Liu, *J. Phys. Chem. C*, 2008, **112**, 11286–11289.
16 H. Kim and J. Cho, *J. Mater. Chem.*, 2008, **18**, 771–775.
17 C. H. Xu, J. Sun and L. Gao, *J. Mater. Chem.*, 2012, **22**, 975–979.
18 L. W. Ji, Z. Lin, B. K. Guo, A. J. Medford and X. W. Zhang, *Chem.–Eur. J.*, 2010, **16**, 11543–11548.
19 Y. Wang, M. Wu, Z. Jiao and J. Y. Lee, *Chem. Mater.*, 2009, **21**, 3210–3215.
20 S. J. Ding, J. S. Chen and X. W. Lou, *Adv. Funct. Mater.*, 2011, **21**, 4120–4125.
21 Z. X. Yang, G. D. Du, Z. P. Guo, X. B. Yu, Z. X. Chen, T. L. Guo and R. Zeng, *Nanoscale*, 2011, **3**, 4440–4447.
22 Z. X. Yang, G. D. Du, C. Q. Feng, S. A. Li, Z. X. Chen, P. Zhang, Z. P. Guo, X. B. Yu, G. N. Chen, S. Z. Huang and H. K. Liu, *Electrochim. Acta*, 2010, **55**, 5485–5491.
23 Z. Yang, G. Du, Q. Meng, Z. Guo, X. Yu, Z. Chen, T. Guo and R. Zeng, *J. Mater. Chem.*, 2012, **22**, 5848–5854.
24 L. Ji and X. Zhang, *Electrochem. Commun.*, 2009, **11**, 795–798.
25 L. Ji, A. J. Medford and X. Zhang, *J. Mater. Chem.*, 2009, **19**, 5593–5601.
26 C. Kim, K. S. Yang, M. Kojima, K. Yoshida, Y. J. Kim, Y. A. Kim and M. Endo, *Adv. Funct. Mater.*, 2006, **16**, 2393–2397.
27 N. Ohtsu, N. Masahashi, Y. Mizukoshi and K. Wagatsuma, *Langmuir*, 2009, **25**, 11586–11591.
28 S. B. Amor, G. Baud, M. Benmalek, H. Dunlop, R. Frier and M. Jacquet, *J. Adhes.*, 1998, **65**, 307–329.

29 Y. S. Su, M. Y. Lee and S. D. Lin, *Catal. Lett.*, 1999, **57**, 49–53.
30 J. Yang, H. Bai, X. Tan and J. Lian, *Appl. Surf. Sci.*, 2006, **253**, 1988–1994.
31 XPS database on the web: http://www.lasurface.com/database/elementxps.php, April 2013.
32 D. Haridas, K. Sreenivas and V. Gupta, *Sens. Actuators, B*, 2008, **133**, 270–275.
33 R. Zhang, H. Wu, D. Lin and W. Pan, *J. Am. Ceram. Soc.*, 2009, **92**, 2463–2466.
34 D. Deng, M. G. Kim, J. Y. Lee and J. Cho, *Energy Environ. Sci.*, 2009, **2**, 818–837.
35 J. S. Chen and X. W. Lou, *Electrochem. Commun.*, 2009, **11**, 2332–2335.
36 N. A. Milne, M. Skyllas-Kazacos and V. Luca, *J. Phys. Chem. C*, 2009, **113**, 12983–12995.
37 C. A. Bonino, L. Ji, Z. Lin, O. Toprakci, X. Zhang and S. A. Khan, *ACS Appl. Mater. Interfaces*, 2011, **3**, 2534–2542.
38 B. Guo, Y. Li, Y. Yao, Z. Lin, L. Ji, G. Xu, Y. Liang, Q. Shi and X. Zhang, *Solid State Ionics*, 2011, **204–205**, 61–65.
39 J. Liu, Y. Wan, C. Liu, W. Liu, S. Ji, Y. Zhou and J. Wang, *Eur. J. Inorg. Chem.*, 2012, **2012**, 3825–3829.
40 X. Chen, X. Li, F. Ding, W. Xu, J. Xiao, Y. Cao, P. Meduri, J. Liu, G. L. Graff and J.-G. Zhang, *Nano Lett.*, 2012, **12**, 4124–4130.
41 L. Ji, Z. Lin, M. Alcoutlabi and X. Zhang, *Energy Environ. Sci.*, 2011, **4**, 2682–2699.
42 J. Jiang, Y. Li, J. Liu, X. Huang, C. Yuan and X. W. Lou, *Adv. Mater.*, 2012, **24**, 5166–5180.